

Receiver function analysis

We use high signal-to-noise ratio (> 10) broadband seismic recordings from 369, $M > 6$ earthquakes at teleseismic distances that occurred between 2002 and 2006. Three-component seismograms are decomposed into P and S upgoing wave modes and deconvolved using Wiener spectral deconvolution to obtain radial and transverse P receiver functions (RFs). At each station we used an average of 100 highest quality RFs which were sorted by back-azimuth of incident wavefield and filtered at corner frequencies of 0.05 to 0.5 Hz, 0.05 Hz to 1 Hz, and 0.05 Hz to 2 Hz (Fig. S1). The resulting RFs show coherent signals representing direct P-to-S (Ps) conversions and free-surface P-to-S (Pps) and S-to-S (Pss) reverberations from velocity contrasts (Fig. S2) within the underlying column that are most easily seen at lower frequencies (Fig. S1A). Each scattered phase displays oppositely-polarized (blue-red for Ps and Pps, red-blue for Pss) pulses that are characteristic of a prominent, dipping low-velocity layer.

Phase weighted stacking

The timing of scattered modes (Ps, Pps, Pss) relative to P can be employed to estimate depth and dip of major interfaces, and the average V_P/V_S of the overlying column^{1,2}, by stacking moveout-corrected RFs using a range of models and identifying which model produces the maximum constructive interference. Strike direction (N45W) is constrained by polarity reversals on transverse

RFs. We adopt the phase-weighted stacking technique of Schimmel³ but employ the median instead of the mean to improve stack coherency. Our first target is the positive velocity contrast representing the Moho of the subducted oceanic plate⁴. We use a dipping, single-layer model with mantle and crustal P velocities of 7.8 and 6.5 km/s⁵ to compute travel-times, although the results are only weakly dependent on this assumption⁶. Our results suggest that the material overlying the oceanic Moho (oceanic crust + continental crust) has a vertically-averaged V_P/V_S of 1.82 ± 0.07 for the range of stations along the array (Fig. S3). On the stacks, the strong negative trough corresponding to the top of low-velocity oceanic crust appears at shallower depths with an average V_P/V_S of overlying material (continental crust) of 1.73 ± 0.07 along the array that is consistently lower by an average of 0.09 than V_P/V_S of material overlying the oceanic Moho. Discrepancy in the average V_P/V_S of the overlying column suggests that the low-velocity layer bounded by both discontinuities has significantly higher V_P/V_S than overlying material. The vertical thickness of the low-velocity layer is approximately constant along the array and has mean value of 4.6 ± 1.1 km.

Based on these findings we further investigate the structure of the low-velocity layer by studying the relative travel-times between positive and negative signals for each scattered phase.

Auto-correlation stacking

We adopt a similar stacking methodology to characterize the layer interval Poisson's ratio by incorporating a few modifications. In the usual stacking approach¹ travel-times are computed relative

to an absolute 0 time that is conveniently provided through deconvolution. V_P/V_S for the low-velocity layer is sensitive to relative travel-time differences from two scattered arrivals (for a given scattering mode) originating at the top and bottom of that layer. We obtain time series of differential S-phase time lags by extracting oppositely-polarized pulses from filtered RF windows for a given scattering mode centered around the solution for the oceanic Moho found previously, and calculating the normalized auto-correlation (Fig. S4, S5). All positive peaks are zeroed out to eliminate interference from arrivals that do not conform with the LVZ model, and the auto-correlations are shifted and stacked using travel-time expressions for a dipping, low-velocity layer with fixed dip and P and S velocity estimates for both underlying and overlying media (Fig. S6).

The stacking approach benefits from efficient computation of travel-times through dipping layer models. In the next section we develop analytic expressions for plane-wave travel-times that avoid solution of an eigenvalue problem⁷.

Plane-wave travel-times

Let us consider the propagation of a plane P-wave incident from below upon a stack of planar, dipping (and not necessarily parallel) layers. The timing of the Ps phase from the L^{th} and $L + 1^{st}$ interfaces can be written as (see Frederiksen⁷)

$$t_{Ps}^L = \sum_{i=1}^L \Delta z_i [\hat{\xi}_i^S - \hat{\xi}_i^P] \quad (1)$$

$$t_{Ps}^{L+1} = \sum_{i=1}^{L+1} \Delta z_i [\hat{\xi}_i^S - \hat{\xi}_i^P], \quad (2)$$

respectively, where $\hat{\xi}_i$ is the absolute value of the vertical component of slowness of the appropriate (P or S) upgoing wave in the i^{th} layer, and Δz_i is layer thickness. The differential travel-time $\Delta t_{P_s}^L$ between two Ps conversions from the top and bottom of the L^{th} layer is thus

$$\Delta t_{P_s}^L = \Delta z_L [\hat{\xi}_L^S - \hat{\xi}_L^P]. \quad (3)$$

Similar expressions hold for Pps and Pss reverberations, namely

$$\Delta t_{Pps}^L = \Delta z_L [\hat{\xi}_L^S + \check{\xi}_L^P] \quad (4)$$

$$\Delta t_{Pss}^L = \Delta z_L [\hat{\xi}_L^S + \check{\xi}_L^S], \quad (5)$$

where $\check{\xi}$ signifies absolute value of vertical component of slowness for a downgoing wave. In a 1-D medium, these expressions simplify to

$$\Delta t_{P_s}^L = \Delta z_L \left[\sqrt{R_L^2/V_{P,L}^2 - p^2} - \sqrt{1/V_{P,L}^2 - p^2} \right] \quad (6)$$

$$\Delta t_{Pps}^L = \Delta z_L \left[\sqrt{R_L^2/V_{P,L}^2 - p^2} + \sqrt{1/V_{P,L}^2 - p^2} \right] \quad (7)$$

$$\Delta t_{Pss}^L = \Delta z_L \left[2\sqrt{R_L^2/V_{P,L}^2 - p^2} \right], \quad (8)$$

where p is horizontal slowness of the incident wavefield, and $R = V_P/V_S$ of the layer. Note that only two equations are independent in this case since $\Delta t_{Pss}^L = \Delta t_{P_s}^L + \Delta t_{Pps}^L$.

For a planar dipping layer with parallel boundaries and unit normal $\mathbf{n} = (n_1, n_2, n_3)$, these expressions generalize to

$$\Delta t_{P_s}^L = n_3 \Delta z_L \left[\sqrt{\frac{R^2}{V_{P,L}^2} - \frac{1}{V_{P,L+1}^2} + (\mathbf{n} \cdot \mathbf{p}^I)^2} - \sqrt{\frac{1}{V_{P,L}^2} - \frac{1}{V_{P,L+1}^2} + (\mathbf{n} \cdot \mathbf{p}^I)^2} \right] \quad (9)$$

$$\Delta t_{Pps}^L = n_3 \Delta z_L \left[\sqrt{\frac{R^2}{V_{P,L}^2} - \frac{1}{V_{P,L-1}^2} + (\mathbf{n} \cdot \mathbf{p}^R)^2} + \sqrt{\frac{1}{V_{P,L}^2} - \frac{1}{V_{P,L-1}^2} + (\mathbf{n} \cdot \mathbf{p}^R)^2} \right] \quad (10)$$

$$\Delta t_{P_{ss}}^L = 2n_3 \Delta z_L \left[\sqrt{\frac{R^2}{V_{P,L}^2} - \frac{1}{V_{S,L-1}^2} + (\mathbf{n} \cdot \mathbf{p}^S)^2} \right], \quad (11)$$

where the slowness vectors \mathbf{p}^I , \mathbf{p}^R , \mathbf{p}^S correspond to the incident P-wave below the layer, the free-surface reflected P-wave above the layer and the free-surface reflected S-wave above the layer, respectively. \mathbf{p}^R and \mathbf{p}^S are computed by applying Snell's law across the interfaces. These travel-times depend on the assumed background velocity model, but, as before, only weakly.

Limiting cases

To characterize R (or Poisson's ratio) within the layer the key parameter is the ratio between Δt_{P_s} and $\Delta t_{P_{ps}}$ (or $\Delta t_{P_{ss}}$). Consider a single, horizontal layer located within an otherwise homogeneous half-space, and a normally-incident plane P-wavefield (ignoring for a moment that no conversions are generated in such a circumstance). In this case the ratio of equations (6) and (7) is independent of V_P and Δz , and yields

$$X \equiv \frac{\Delta t_{P_s}}{\Delta t_{P_{ps}}} = \frac{(R-1)}{(R+1)}. \quad (12)$$

Solving for R we have

$$R = \frac{1+X}{1-X}. \quad (13)$$

As X tends to zero (i.e. Δt_{P_s} tends to 0 or $\Delta t_{P_{ps}} \gg \Delta t_{P_s}$), R tends to 1, and $V_P \rightarrow V_S$. As X tends to one (i.e. $\Delta t_{P_s} \rightarrow \Delta t_{P_{ps}}$), R tends to ∞ , and $V_S \rightarrow 0$.

Poisson's ratio (σ) is calculated from R using

$$\sigma = \frac{1}{2} \left[1 - \frac{1}{R^2 - 1} \right] \quad (14)$$

Frequency bias

To avoid bias in the determination of R , one must be careful not to low-pass filter RFs at corner periods larger than twice the true time separation between pulses (Fig. S7). If Δt_{Ps} is biased to higher values (i.e. cutoff frequency is too low), both X and R will be biased upward. The opposite relation is true for the reverberations. For example, if Δt_{Pps} is biased upward, both X and R will be biased downward. It is thus crucial that the time series for Ps be filtered at frequencies high enough to resolve the smallest differential travel-times between the oppositely-polarized signals. Using synthetic tests we verified that a cutoff frequency of 2 Hz is appropriate and sufficient for our purposes. Because Pps and Pss reverberations are more band-limited, we use a cutoff frequency of 1 Hz. Using slightly lower cutoff frequencies for Pps and Pss will not affect the recovery of R because X is always smaller than 1, moreover, any bias will yield more conservative estimates of V_P/V_S .

Bootstrapping

Standard errors are calculated using the bootstrap method⁸. For each set of receiver functions (or auto-correlations) we randomly resample the original data set with replacement and perform phase-weighted stacking. A best fit value is determined for the resampled data set and this procedure is repeated 100 times to calculate the standard deviation around the solution.

1. Zhu, L. and Kanamori, H. Moho depth variation in southern California from teleseismic receiver functions. *J. Geophys. Res.* **105**, 2969–2980 (2000).
2. Rossi, G., Abers, G. A., Rondenay, S., and Christensen, D. H. Unusual mantle Poisson's ratio, subduction, and crustal structure in central Alaska. *J. Geophys. Res.* **111**, B09311, doi:10.1029/2005JB003956 (2006).
3. Schimmel, M. and Paulssen, H. Noise reduction and detection of weak, coherent signals through phase-weighted stacks. *Geophys. J. Int.* **130**, 497–505 (1997).
4. Abers, G. A. Seismic low-velocity layer at the top of subducting slabs beneath volcanic arcs: observations, predictions, and systematics. *Phys. Earth Planet. Int.* **149**, 7–29, doi:10.1016/j.pepi.2004.10.002 (2005).
5. Ramachandran, K., Hyndman, R. D., and Brocher, T. M. Regional *p* wave velocity structure of the Northern Cascadia Subduction Zone. *J. Geophys. Res.* **111**, B12301, doi:10.1029/2005JB004108 (2006).
6. Zandt, G. and Ammon, C. J. Continental crust composition constrained by measurements of crustal Poisson's ratio. *Nature* **374**, 152–154 (1995).
7. Frederiksen, A. W. and Bostock, M. G. Modelling teleseismic waves in dipping anisotropic structures. *Geophys. J. Int.* **141**, 401–412 (2000).
8. Efron, B. and Tibshirani, R. Statistical data analysis in the computer age. *Science* **253**, 390–395 (1991).

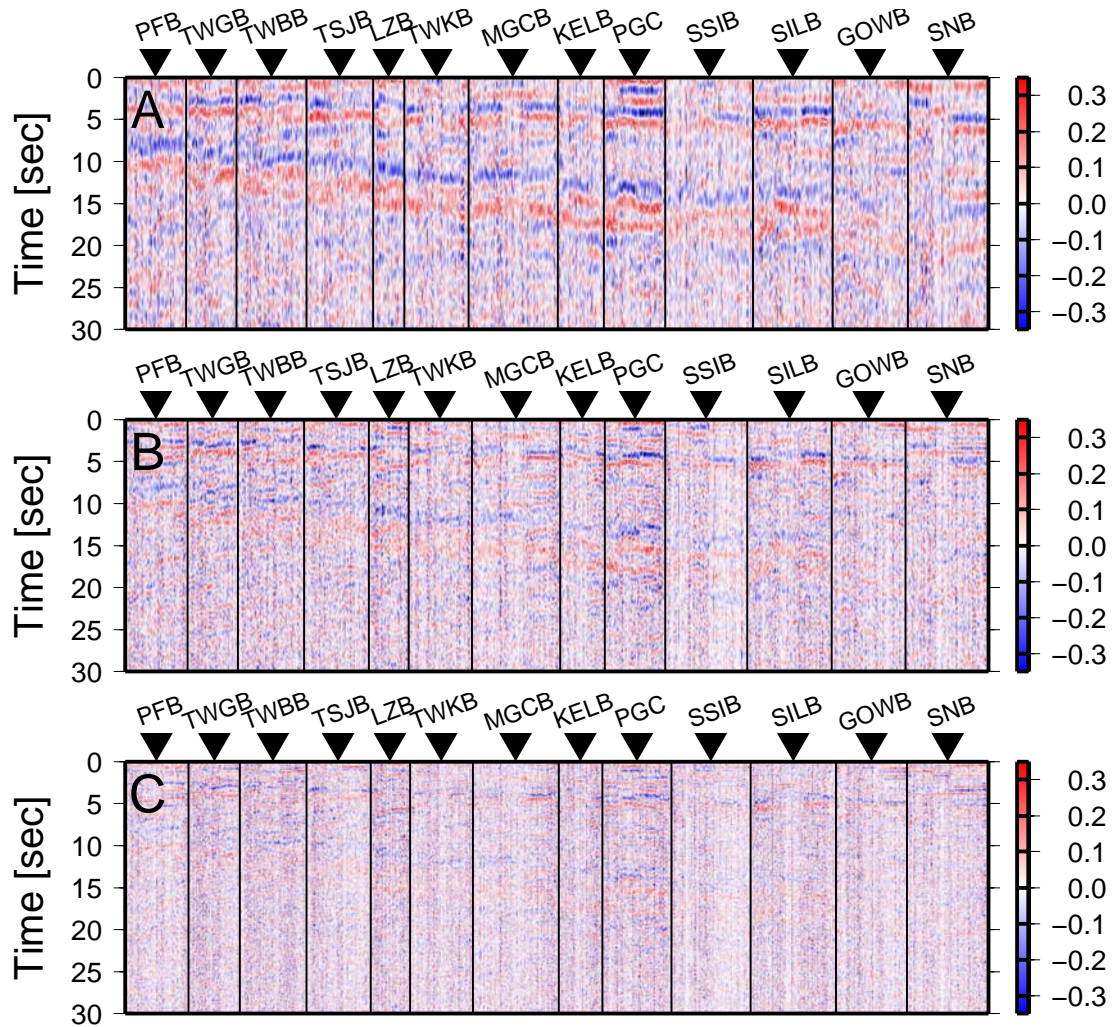


Figure S1. Receiver functions for all data used in the analysis sorted by station position along the line and, for each station, by back-azimuth of incident wavefield. Receiver functions are filtered at cutoff frequencies of: **A)** 0.05 - 0.5 Hz; **B)** 0.05 - 1 Hz; **C)** 0.05 - 2 Hz. Only data from **B)** and **C)** are used in the analysis; **A)** is plotted for visual purposes. Amplitudes are relative to incident P wave. Note that distances are not preserved on this plot.

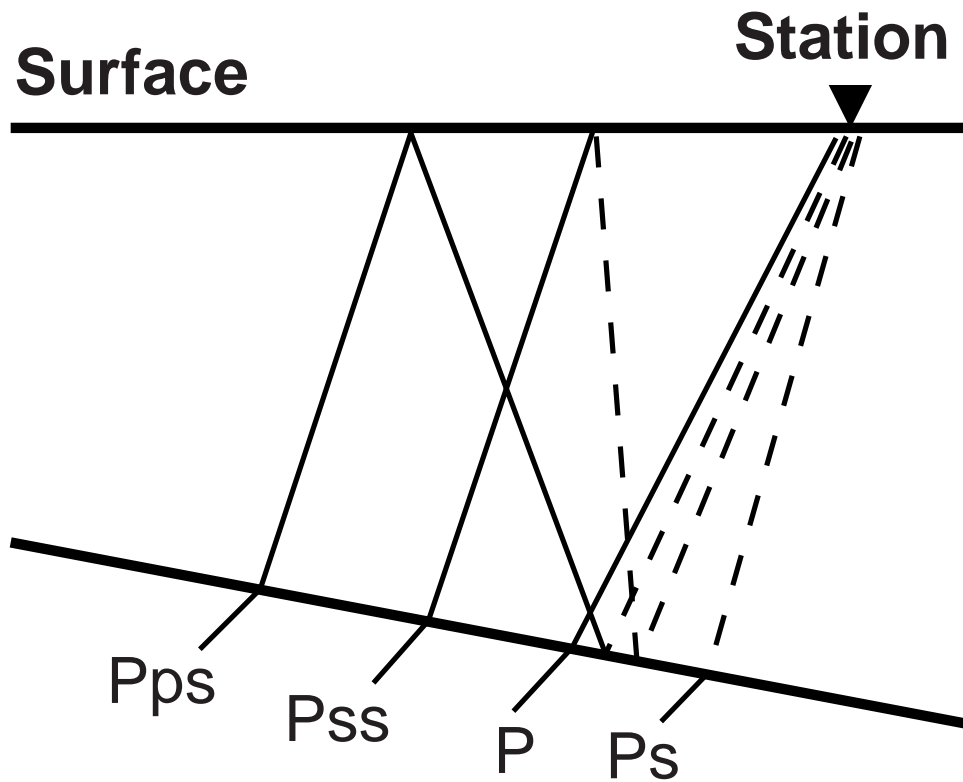


Figure S2. Ray diagram for P-to-S converted phases and free-surface multiples from a single dipping interface, for example the oceanic Moho. Rays travelling as P waves are represented by solid lines, whereas rays representing S travelling waves are shown as dashed lines. For a dipping, low-velocity layer bounded by parallel interfaces, this set of wave conversions is generated twice with opposite polarities for waves scattered at the top and bottom layer boundaries, as in Fig. S2

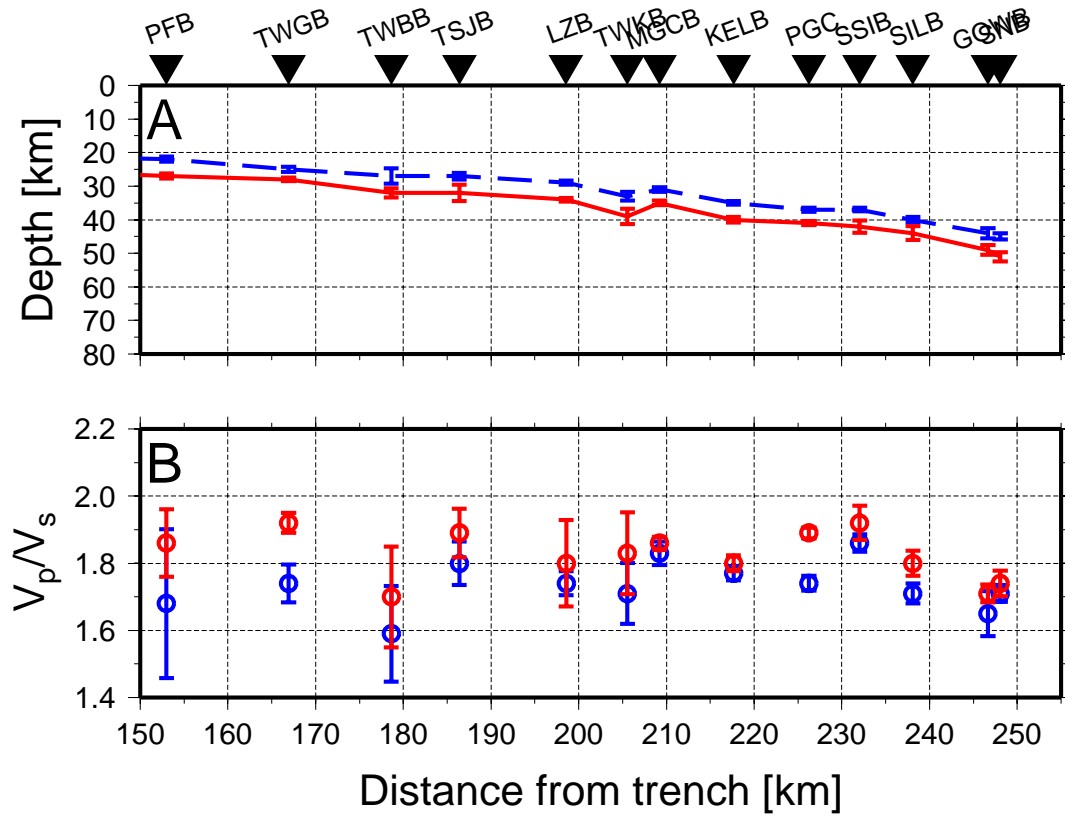


Figure S3. Depth (A) to top and bottom interface and V_p/V_s (B) of overlying column obtained by stacking receiver functions filtered between 0.05 - 1 Hz.

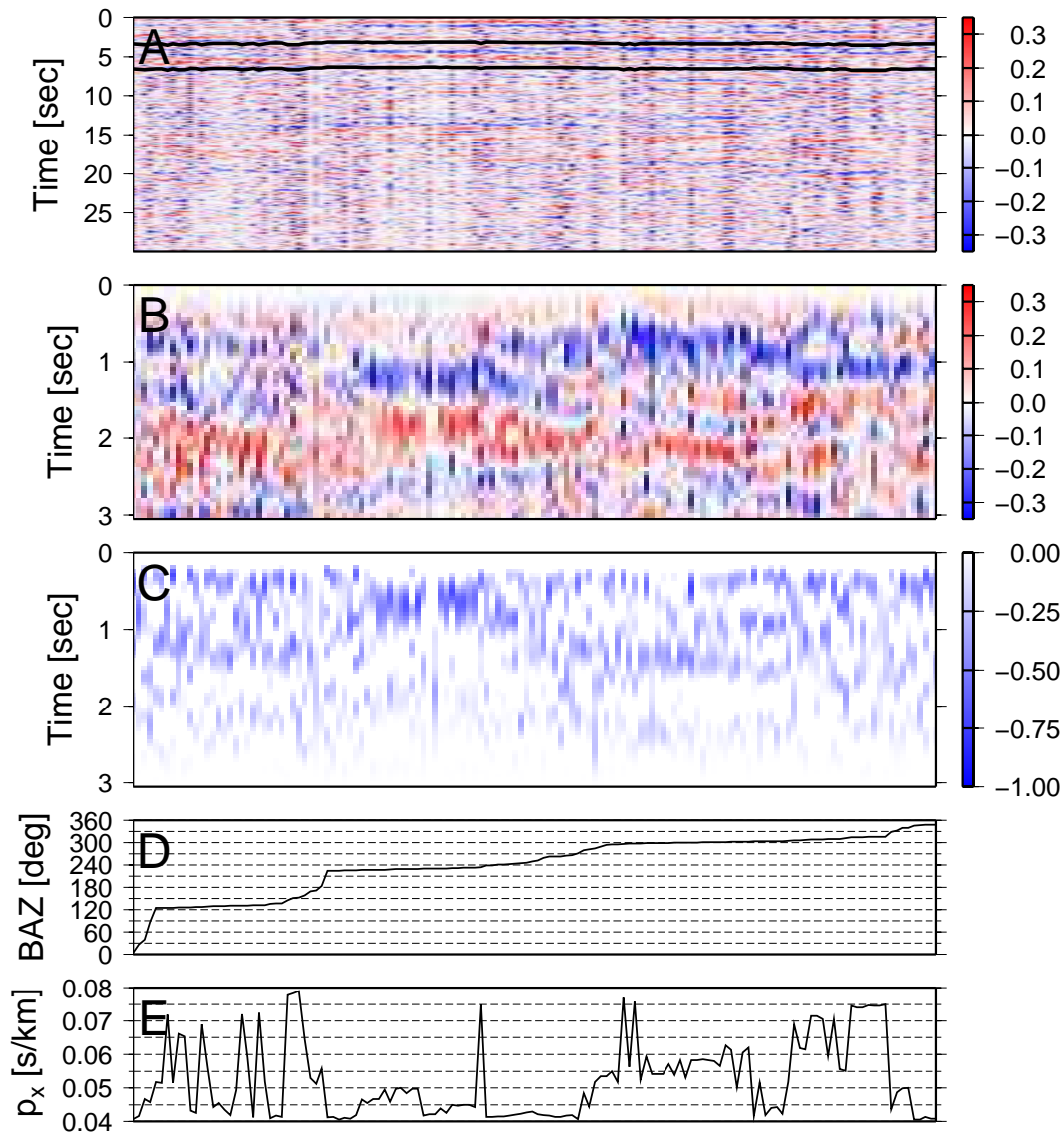


Figure S4. Window extraction and auto-correlation of Ps phase filtered with cutoff frequency of 2 Hz at station PGC. In **A**) a window (bounded by black lines) is chosen on the basis of predicted Ps arrival times for the subducted oceanic Moho (Fig. S2). The extracted window (**B**) is tapered and autocorrelated (**C**). Each autocorrelation is normalized by positive peak amplitude at 0 time (not shown here) and all positive peaks are subsequently zeroed out. **D**) and **E**) show the back-azimuthal and horizontal slowness distribution of incident wavefields for each corresponding trace plotted in **A**).

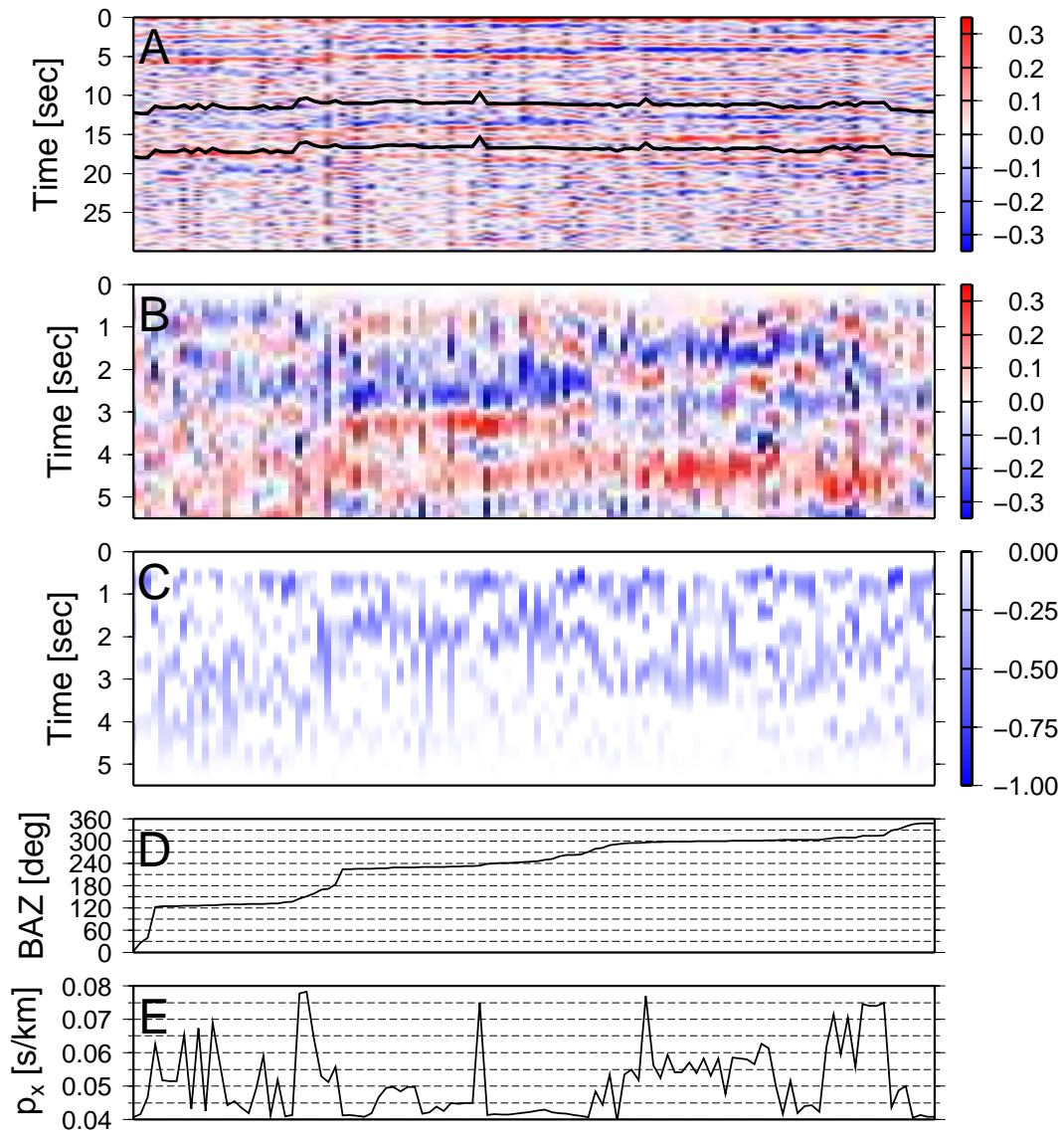


Figure S5. Same as Fig. S3 for Pps phase and cutoff frequency of 1 Hz at station PGC.

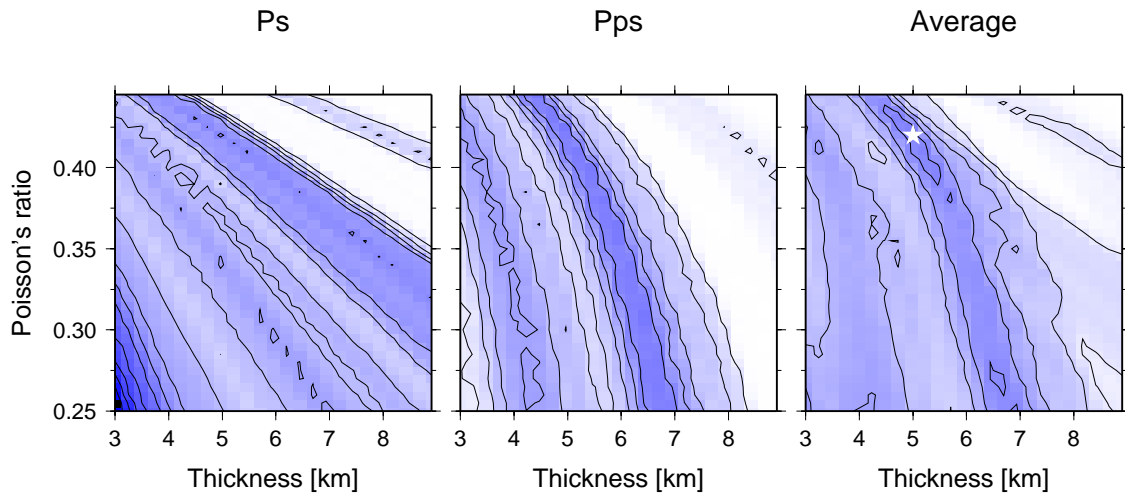


Figure S6. Autocorrelation stacking results for station PGC. We use only Ps and Pps phases from Fig. S3 and Fig. S4 because Pss auto-correlations are not coherent at 1 Hz. Each phase is given equal weight and the minimum of the averaged stack gives the estimated Poisson's ratio and thickness of low-velocity layer.

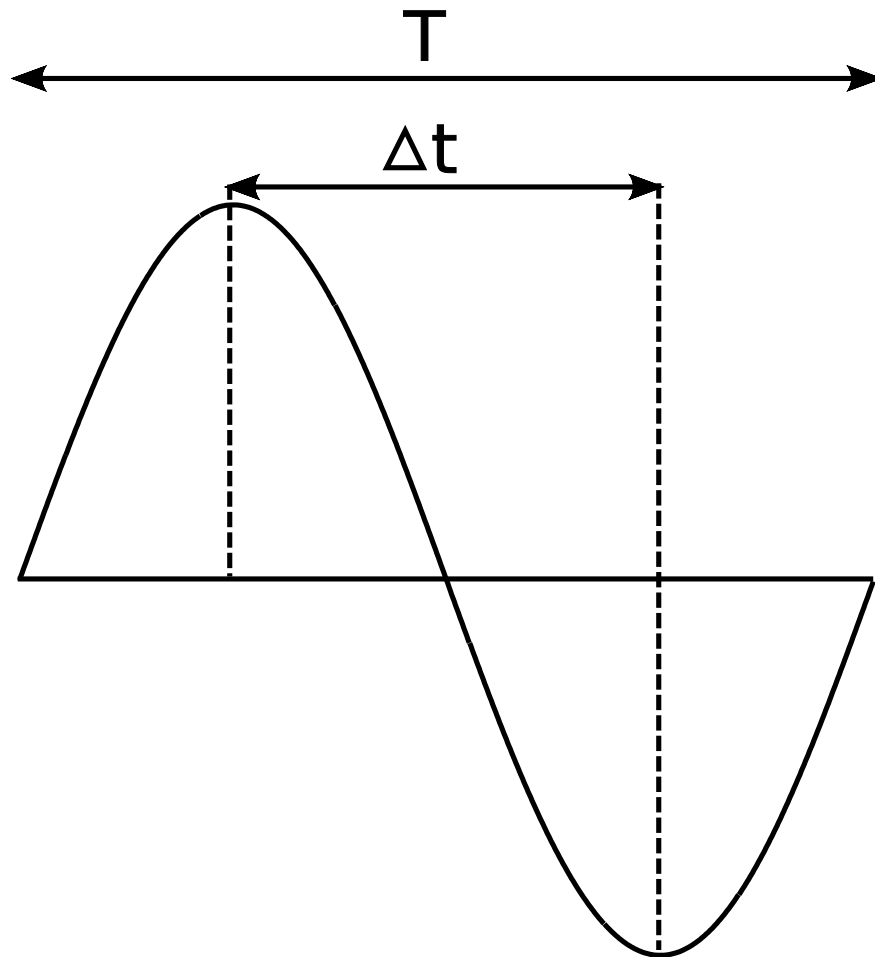


Figure S7. Illustration of frequency bias due to filtering. T is corner period of filter, Δt is minimum value of recovered time difference.